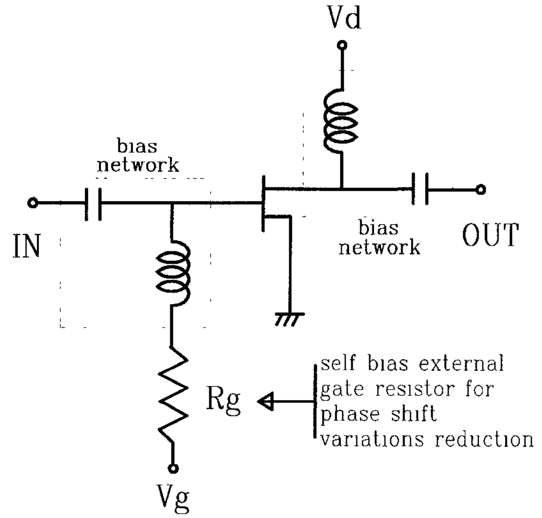

Fig. 7. Implementation of a self-bias gate resistor R_g in the bias network for phase distortion minimization.

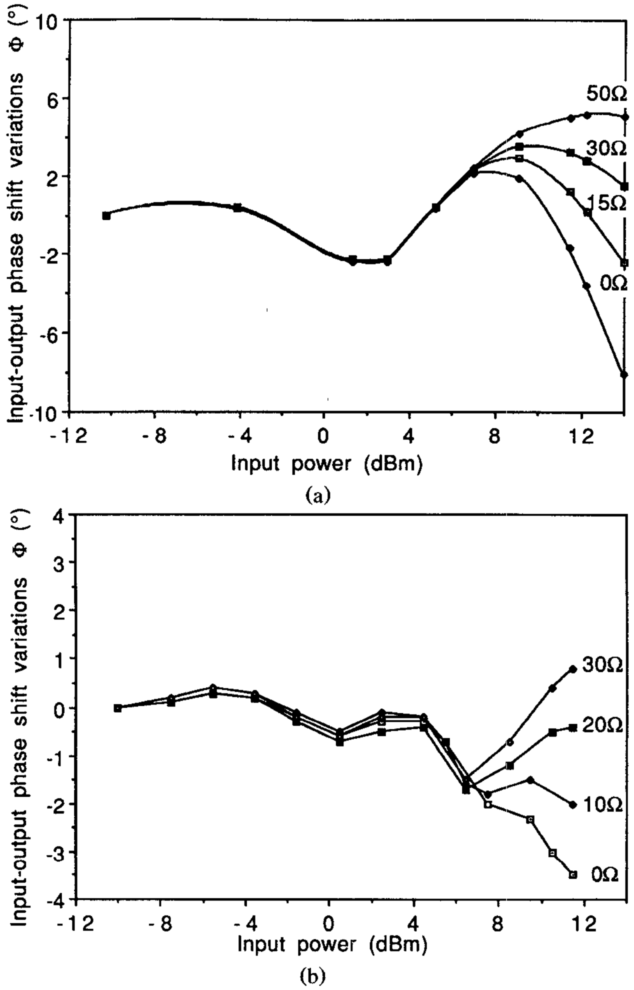

(a)

(b)

Fig. 8. (a) Simulated phase shift variations Φ versus input power with the value of the self-bias resistor R_g as parameter. A value of R_g in the 20 Ω range provides the lowest phase distortion for the considered device. (b) Measured phase shift variations Φ versus input power for different values of the self-bias gate resistor R_g. As predicted by simulations, a value for R_g near 20 Ω provides the lowest phase distortion.

To conclude, it may be stated that low phase distortion GaAs MESFET limiters can be designed provided that the FET used in the limiter features a gate built-in voltage as large as possible (a correct value is in excess of 0.75 V, which is classical for GaAs FET) and that a self-bias gate series resistor is used at an appropriate value. These two conditions can be easily satisfied, especially in MMIC implementations.

ACKNOWLEDGMENT

The authors would like to thank S. Bertrand (Alcatel Espace) for suggesting this work, L. Lapierre (CNES) and M. Camiade (Thomson-DHM) for their authorization to use some of their characterization tools, and J. Rayssac for technical assistance.

REFERENCES

[1] S. Bertrand, "Amplificateur-limiteur à TEC sans déphasage. Applications dans la bande 7.9–8.4 GHz," *Journées Nationales Microondes de Nice*, 1987, pp. 146–147, June 1987.
[2] H. Fukui, "Determination of the basic device parameters for a GaAs MESFET," *Bell Syst. Tech. J.*, vol. 58, no. 3, Mar. 1979.
[3] M. Gayral *et al.*, "A general method for the analysis of non linear microwave circuits," in *IEEE MTT-S Int. Microwave Symp. Dig.*, June 1987, pp. 119–121.
[4] W. R. Curtice, "A MESFET model for use in the design of GaAs integrated circuit," *Trans. Microwave Theory Tech.*, vol. MTT-28, May 1980.
[5] W. R. Curtice, "A non-linear GaAs FET model for use in the design of output circuit for power amplifiers," *Trans. Microwave Theory Tech.*, vol. MTT-33, Dec. 1985.
[6] Y. Tajima, "GaAs FET large signal model and its application to circuit design," *IEEE Trans. Electron Devices*, vol. ED-28, Feb. 1981.
[7] A. Materka, "Computer calculation of large signal GaAs FET amplifier characteristic," *Trans. Microwave Theory Tech.*, vol. MTT-33, Feb. 1985.
[8] H. Statz, "GaAs FET device and circuit simulation in SPICE," *IEEE Trans. Electron Devices*, vol. ED-34, Feb. 1987.
[9] I. Telliez, B. Carnez, M. Gayral, and C. Rumelhard, "Modélisation grand signal de TEC pour la simulation de Circuits Intégrés Monolithiques Hyperfréquences en GaAs," *Journées Nationales Microondes de Nice*, pp. 230–232, June 1987.
[10] J. W. Bandler, "A unified framework for harmonic balance simulation sensitivity analysis," in *IEEE MTT-S Int. Microwave Dig.*, June 1988.
[11] M. Paggi, "Nonlinear GaAs MESFET modelling using pulsed gate measurement," in *IEEE MTT-S Int. Microwave Symp. Dig.*, June 1988.
[12] J. F. Vidalou, "On-wafer large signal pulsed measurements," in *IEEE MTT-S Int. Microwave Symp. Dig.*, June 1989, pp. 831–834.

An Approach to Microwave Imaging Using a Multiview Moment Method Solution for a Two-Dimensional Infinite Cylinder

S. Caorsi, G. L. Gragnani, and M. Pastorino

***Abstract*—An approach based on a multiview solution to the inverse-scattering problem of a two-dimensional infinite cylinder is developed in a space–frequency domain. Microwave imaging is simulated by a com-**

Manuscript received May 10, 1990; revised December 3, 1990.
The authors are with the Department of Biophysical and Electronic Engineering, University of Genoa, Via all'Opera Pia 11/a, 16145 Genoa, Italy.
IEEE Log Number 9042498.

puter algorithm using the moment method. To overcome ill-conditioning and solve nonsquare systems, a pseudoinverse transformation is employed. The equivalent current density and the complex conductivity are considered as object functions for image formation. The results of some numerical simulations in a noisy environment are reported, and a discussion of monoview and multiview imaging techniques for a space–frequency domain is presented.

I. Introduction

In the past few years, there has been a growing interest in microwave imaging [1]–[3]. However, concerned about the complexity of the mathematical models involved in microwave imaging processes, researchers are currently working on the development of simple, yet efficient and reliable, imaging systems. In the past, several algorithms based on the well-known Fourier diffraction projection theorem were developed. Since such algorithms are generally based on Born's or Rytov's approximations, they have been successfully utilized in the case of weakly scattering objects. However, they usually fail when applied to strong scatterers [4].

In recent years, other techniques have been developed to image strong scatterers in a simple way. Algorithms based on the inversion of the integral electromagnetic scattering equation for a space–frequency domain, using the moment method [5], have been presented [6]–[11]. However, while multiview algorithms are commonly used in diffraction tomography, most space-domain algorithms have so far been applied to monoview measurements, even though the theories developed in some of these works [8], [10]–[12] do not exclude the possibility of suitably utilizing multiview systems.

In the present work, a multivision algorithm using the moment method is developed in a two-dimensional case. The approach is based on the use of an illuminating electromagnetic source that rotates jointly with the observation domain where the scattered electromagnetic field is measured. The numerical solution to the moment method formulation is reached by means of a pseudoinversion [7], [13]. Because of the joint rotation of the illuminating source with the observation domain, the pseudoinverse matrix can be evaluated off line once and for all; therefore, the reconstruction process is developed, view by view, through a fast matrix-by-vector product. The results of some numerical simulations are presented, discussed, and compared with those obtained in monoview cases and for noisy data.

II. Mathematical Formulation

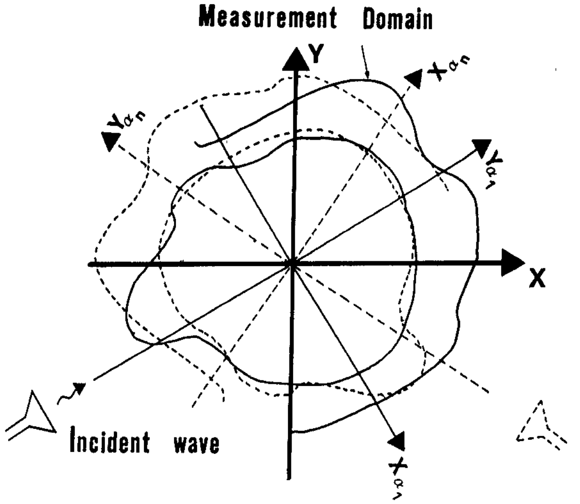

Fig. 1. Problem geometry.

We start by using the formulation for 2-D direct TM scattering [14]. We assume an investigation domain, I_d, that is the cross section of an infinitely long cylinder with a complex conductivity:

$$\tau(x,y)=\sigma(x,y)+j\omega\epsilon[\epsilon_r(x,y)-1] \tag{1}$$

which represents the final problem unknown in the inverse procedure. The investigation domain is illuminated by a known incident electric field, $E^i_{\alpha_1}$, polarized along the cylinder axis and propagating in the y_{α_1} direction (perpendicular to the cylinder axis). The resulting scattered electric field, $E^s_{\alpha_1}$, and the total electric field, $E^t_{\alpha_1}$, are also polarized along the cylinder axis. The electric field integral equation suitable for this problem is given as follows (it is worth pointing out that for TE scattering a magnetic field integral equation [15] should be used):

$$E^s_{\alpha_1}(x_{\alpha_1},y_{\alpha_1}) = j\omega\mu\int_{I_d}\tau(x',y')E^t_{\alpha_1}(x',y')\cdot G(x_{\alpha_1},y_{\alpha_1}/x',y')\,dx'dy' \tag{2}$$

where $G(x_{\alpha_1},y_{\alpha_1}/x',y')$ is the 2-D Green function for free space [14]. Relation (2) holds at every point in space, in particular, inside a domain D_{α_1} (outside the investigation domain) where the scattered electric field can be measured.

Let us now rotate the illumination source by N angular positions α_n jointly with the measurement and the investigation domains. (Fig. 1 shows the proposed imaging arrangement.) A set of N integral equations is obtained:

$$E^s_{\alpha_n}(x_{\alpha_n},y_{\alpha_n}) = j\omega\mu\int_{I_d}\tau(x',y')E^t_{\alpha_n}(x',y')G(x_{\alpha_n},y_{\alpha_n}/x',y')\,dx'dy',\qquad n=1,\cdots,N. \tag{3}$$

Solving this set of equations allows one to use multiview information. We use the equivalent current densities

$$J_{\alpha_n}(x',y')=\tau(x',y')E^t_{\alpha_n}(x',y'),\qquad n=1,\cdots,N \tag{4}$$

as intermediate unknowns, so that the following set of integral equations is to be solved:

$$E^s_{\alpha_n}(x_{\alpha_n},y_{\alpha_n}) = j\omega\mu\int_{I_d}J_{\alpha_n}(x',y')G(x_{\alpha_n},y_{\alpha_n}/x',y')\,dx'dy',\qquad n=1,\cdots,N. \tag{5}$$

To solve equations (5), the moment method is adopted; for each angular position α_n $(n=1,\cdots,N)$, we take

$$J_{\alpha_n}(x,y)=\sum_m J^m_{\alpha_n}f^m(x,y),\qquad n=1,\cdots,N \tag{6}$$

where the $J^m_{\alpha_n}$'s are the M coefficients to be determined, and the basis functions $f^1 \cdots f^M$ are the same for each angular position.

By performing the inner products with P testing functions, $w^1(x,y) \cdots w^P(x,y)$, we obtain the following relationships:

$$\left\langle w^p(x_{\alpha_n}, y_{\alpha_n}), E^s_{\alpha_n}(x_{\alpha_n}, y_{\alpha_n})\right\rangle = j\omega\mu \sum_m J^m_{\alpha_n}\left\langle w^p(x_{\alpha_n}, y_{\alpha_n}), f^m(x', y') \cdot G(x_{\alpha_n}, y_{\alpha_n}/x', y')\, dx'\, dy'\right\rangle,$$
$$n = 1, \cdots, N; \quad p = 1, \cdots, P. \tag{7}$$

As the Green function G and the basis functions f^m do not vary with the angular position, relations (7) can be expressed in matrix form:

$$[E^s] = [G][J] \tag{8}$$

where $[G]$ is the $P \times M$ Green matrix, which does not vary with the angular position; $[E^s] = [E^s_{\alpha_1} | E^s_{\alpha_2} | \cdots | E^s_{\alpha_N}]$ is the $P \times N$ matrix whose columns are the N arrays related to the N measures of the scattered electric field; and $[J] = [J_{\alpha_1} | J_{\alpha_2} | \cdots | J_{\alpha_N}]$ is the $M \times N$ matrix whose columns are the N arrays of coefficients of the equivalent current densities at each α_n. To overcome ill-conditioning, the solution to (8) can be achieved via a pseudoinverse transformation [7], [13], thus obtaining

$$[J] = [G]^+[E^s] \tag{9}$$

where $[G]^+$ stands for the pseudoinverse matrix of $[G]$.

For the imaging of weak scatterers, we can use the amplitudes of the equivalent current densities obtained for the various angles of illumination [16]. Since the scattering is weak, if we use an illuminating source with the same amplitude for each α_n, the amplitudes that are obtained for the equivalent current densities are similar and are directly related to the scatterers' dielectric properties. We can form the image by using the mean value of the amplitudes of the equivalent current densities. Then, for each pixel P_{ij} in the final image, we have

$$\text{Level}[P_{ij}] = 1/N \sum_n C^{ij}_n \left[\left| \sum_m J^m_{\alpha_n} f^m(x,y) \right|\right] \tag{10}$$

where the operator C^{ij}_n gives, for the angular position α_n, the correspondence between the coordinate system x, y and the pixel location i, j [12].

To accomplish the dielectric reconstruction, we recall that, for each α_n, the total electric field inside the investigation domain is

$$E^t_{\alpha_n}(x,y) = E^i_{\alpha_n}(x,y) + j\omega\mu \sum_m J^m_{\alpha_n} \int_{I_d} f^m(x', y') G(x, y/x', y')\, dx'\, dy'. \tag{11}$$

Making use of expression (6), the complex conductivity can be obtained as the mean value of the conductivities related to all single views; that is,

$$\tau(x,y) = 1/N \sum_n \frac{\sum_m J^m_{\alpha_n} f^m(x,y)}{E^i_{\alpha_n}(x,y) + j\omega\mu \sum_m J^m_{\alpha_n} \int_{I_d} f^m(x', y') G(x, y/x', y')\, dx'\, dy'}. \tag{12}$$

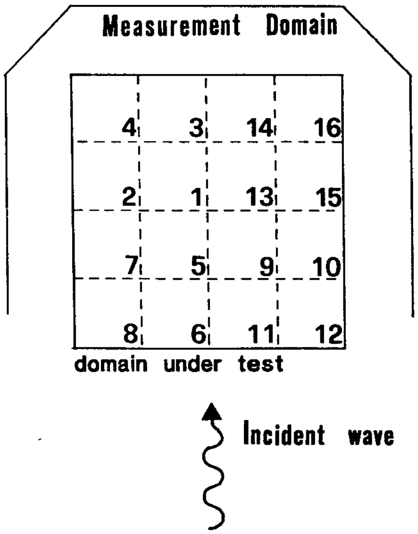

Fig. 2. Geometrical arrangement and cell numbering used for most of the simulations.

It should be stressed that some points may exist for which the total field vanishes, so that the division in (12) becomes indefinite. In practical applications, however, this appears to be a minor problem.

III. Numerical Results and Discussion

Some numerical simulations were performed, with circular cylinders illuminated by an incident plane wave at a frequency of 10 GHz. The scattered electric field was obtained analytically using a well-known series expansion [18]. In the simulations, we used constant subsectional basis functions and Dirac's deltas as testing functions, so that the investigation domain was subdivided into a regular square grid made up of square cells.

In a first set of simulations, we considered a scatterer with $\epsilon_r = 3 - j0$, an investigation domain of λ_0 to a side (subdivided into 16 cells), and 16 measurement points around the investigation domain, as shown in Fig. 2.

One purpose of the simulations was to evaluate the dependence of results on the scatterer's position. Fig. 3 shows four examples, referring to as many monoview imaging processes. The filled circles represent the scattering cylinder (entirely contained in one cell), and the crosses outside each domain mark the locations of the measurement points. In the figure, we give the values of the real parts of the reconstructed dielectric permittivities and the values of the minimum contrasts given by the equivalent current densities and by the real parts of the dielectric permittivities, respectively, defined as

$$\text{CONTR}_J = \frac{|J_{\text{eq}}|_{\text{MAX inside the scatterer}}}{|J_{\text{eq}}|_{\text{MAX outside the scatterer}}} \tag{13}$$

and

$$\text{CONTR}_{\epsilon_r} = \frac{\text{Re}\{\epsilon_r\}_{\text{MAX inside the scatterer}}}{\text{Re}\{\epsilon_r\}_{\text{MAX outside the scatterer}}}. \tag{14}$$

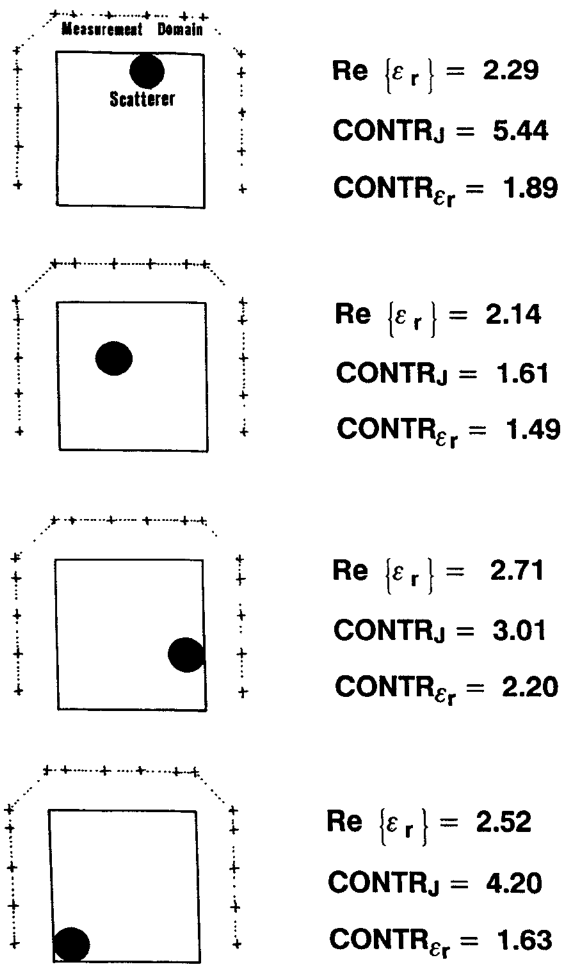

Fig. 3. Results of a monoview reconstruction: values of the real parts of the dielectric permittivity and of the quantities CONTR_J and $\mathrm{CONTR}_{\epsilon_r}$ for four different positions of the scatterer. The filled circle in each investigation domain represents the cylindrical scatterer, and the crosses outside each domain mark the locations of the measurement points. The original value of the dielectric permittivity was $\epsilon_r = 3 - j0$.

The dielectric reconstruction may be more or less accurate, depending on the scatterer's position, since the monoview inversion algorithm is highly sensitive to the array of measures. Accordingly, different positions of the scatterer, giving different measurement values, may result in different degrees of solution accuracy. In any case, the image provided by the equivalent current densities allows an accurate localization of the cylinder. However, whereas in the case of weak scattering the highest contrast is associated with the equivalent current density, in the case of strong scattering the reconstruction of the dielectric permittivity yields higher contrast values.

To verify this assertion, we used the same arrangement, considering a cylinder with $\epsilon_r = 5 - j0$. As can be seen in Fig. 4 (except for one position), the minimum contrast given by the equivalent current density is relatively low. Instead, when a complete dielectric reconstruction was performed, a considerable increase in the contrast value was obtained, together with an accurate dielectric reconstruction of the scatterer.

To evaluate the effect of the scatterer's position on a multiview process, the same simulations performed considering a cylinder with $\epsilon_r = 3 - j0$ were repeated for a reconstruction based on four views, spaced by 90° angles.

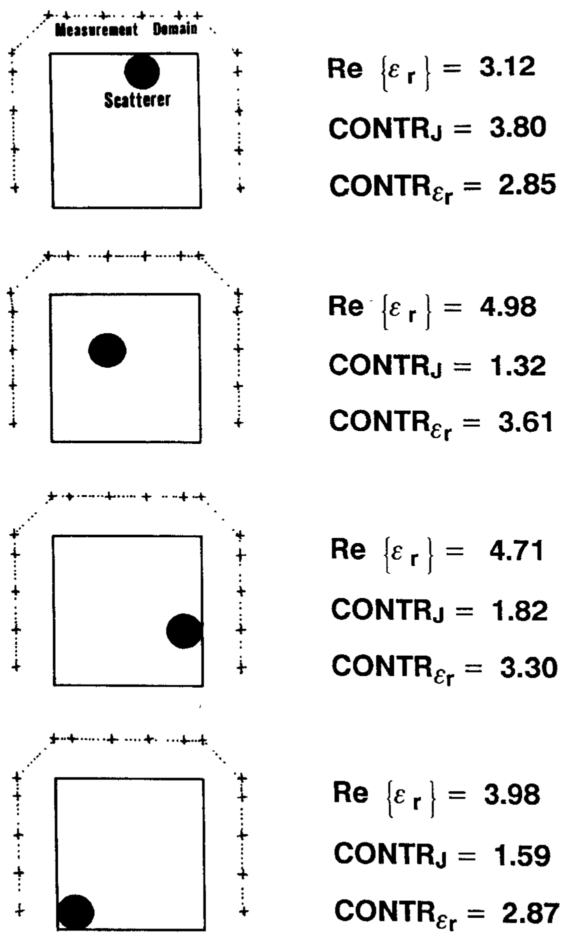

Fig. 4. Results of a monoview reconstruction: values of the real parts of the dielectric permittivity and of the quantities CONTR_J and $\mathrm{CONTR}_{\epsilon_r}$ for four different positions of the scatterer. The filled circle in each investigation domain represents the cylindrical scatterer, and the crosses outside each domain mark the locations of the measurement points. The original value of the dielectric permittivity was $\epsilon_r = 5 - j0$.

The results of such simulations are presented in Fig. 5. Despite a slight loss in contrast, the reconstruction appears much more uniform and less dependent on the scatterer's position. Moreover, an important result (not shown in Fig. 5) lies in the decrease in the effects of ill-conditioning as the number of views increases. This phenomenon can be easily explained by the fact that the multiview algorithm developed includes a space data averaging that has per se a regularizing effect.

Another aspect evaluated via the simulations is the effect of noise. A monoview reconstruction was compared with the corresponding 16-view one. The scatterer was located in the tenth cell, according to the numbering in Fig. 2; the dielectric permittivity was $\epsilon_r = 3 - j0$. Gaussian noise was added to the measures, and for each S/N ratio, 50 reconstruction tests were performed. The parameter that expressed the robustness of the imaging process versus noise (for each S/N ratio) was the following confidence interval:

$$I_c = \frac{|\mathrm{Re}\{\epsilon_r\}_{\mathrm{rec}} - \mathrm{Re}\{\epsilon_r\}_{\mathrm{true}}|_{\mathrm{Max}} - |\mathrm{Re}\{\epsilon_r\}_{\mathrm{rec}} - \mathrm{Re}\{\epsilon_r\}_{\mathrm{true}}|_{\mathrm{min}}}{1/50 \sum_i |\mathrm{Re}\{\epsilon_r\}_{\mathrm{rec}} - \mathrm{Re}\{\epsilon_r\}_{\mathrm{true}}|_i}. \tag{15}$$

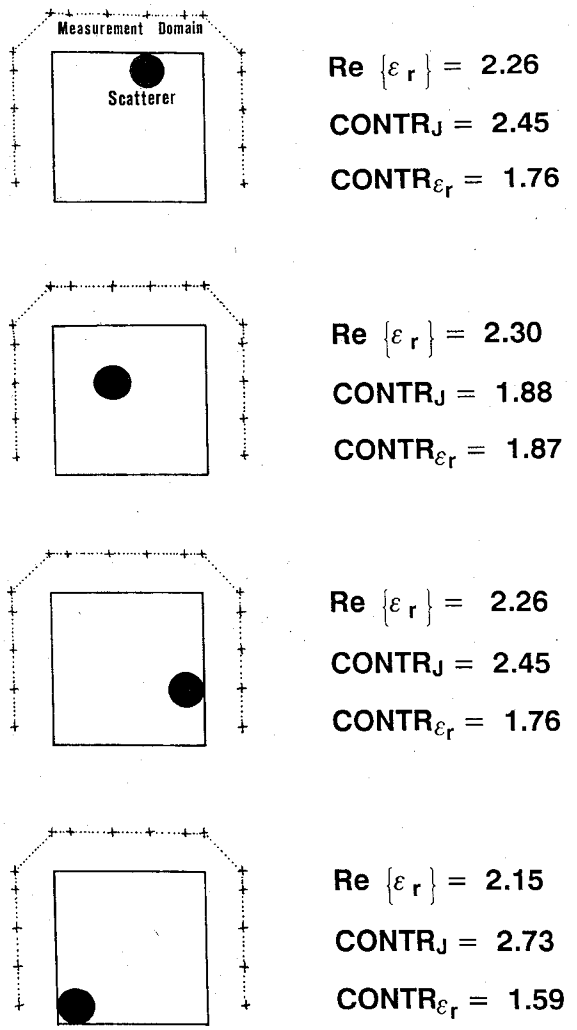

Fig. 5. Results of a four-view reconstruction: values of the real parts of the dielectric permittivity and of the quantities CONTR_J and $\mathrm{CONTR}_{\epsilon_r}$ for four different positions of the scatterer. The filled circle in each investigation domain represents the cylindrical scatterer, and the crosses outside each domain mark the locations of the measurement points. The original value of the dielectric permittivity was $\epsilon_r = 3 - j0$.

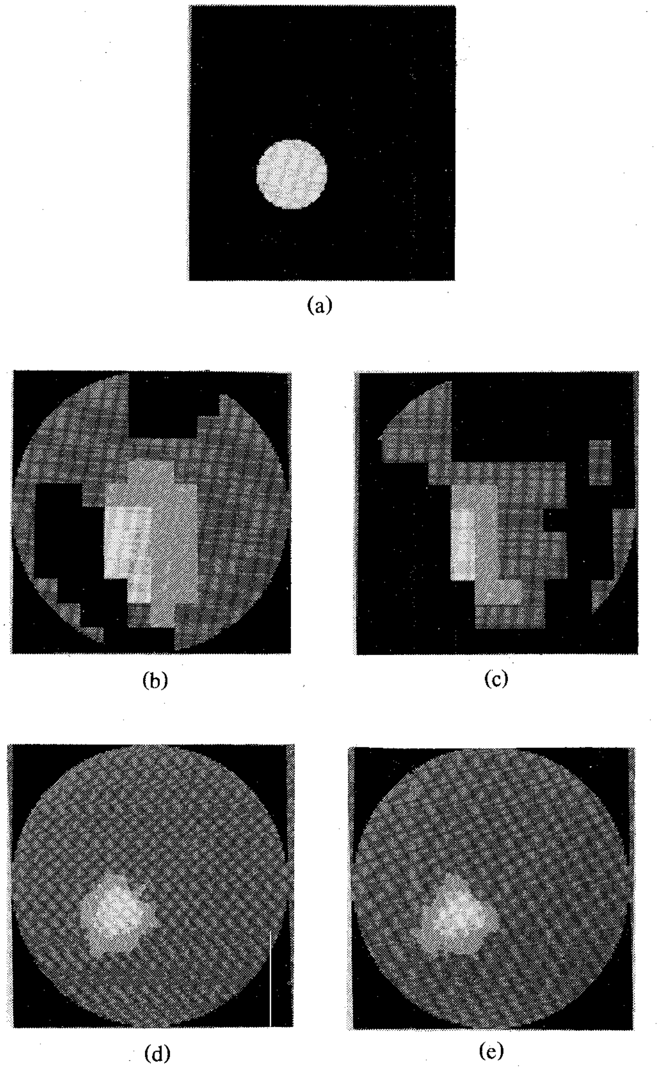
(a)
(b)
(c)
(d)
(e)

Fig. 7. Photographs of the result: (a) scatterer position; (b) reconstruction based on unnoisy measures for a monoview process; (c) reconstruction for S/N = 30 dB for a monoview process; (d) reconstruction based on unnoisy measures for a 32-view process; (e) reconstruction for S/N = 30 dB for a 32-view process.

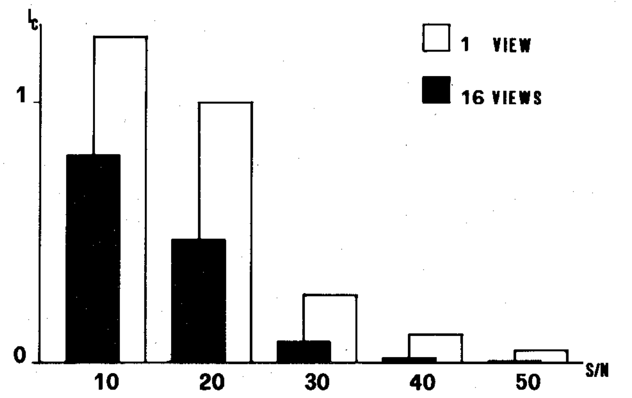

Fig. 6. Histogram showing the values of the parameter I_c for different S/N ratios. White towers refer to monoview processes, and black ones to 16-view processes.

which is the absolute value of the difference between the best and worst values obtained by the 50 tests and normalized to the mean value. As shown by the histogram in Fig. 6, a multiview process allows one to operate, in any case, using I_c values that yield, for each single reconstruction, a constancy of results and a reliability that are definitely higher than those obtainable by a monoview process. Especially for low S/N values, the results yielded by the latter process strongly differ for each reconstruction. Instead, the steady results achieved by a multiview process facilitate the control of ill-conditioning.

Finally, the photographs in Fig. 7 represent, in a pictorial way, the results obtained in a monoview case and in a multiview one (32 equidistant views), for a scatterer with $\epsilon_r = 5 - j0$. In addition, the photographs also show the capability of the approach for using undersized pseudoinverses, which require limited computational resources. This capability was proved by considering a small number of measurement points and a thick discretization of the investigation domain. A domain measuring $\lambda_0 \times \lambda_0$, as in the previous simulations, was subdivided into 144 cells (nine of which were occupied by the scatterer), while the same number of measurement points was used as in the previous simulations (i.e., 16).

Moreover, a comparison between monoview and multiview results highlights the ability of a multiview algorithm to exactly shape a scatterer, whereas in the monoview case, a scatterer's shape may notably vary markedly, depending on the cell size and the position of the scatterer within the cell grid.

As a final remark, we point out that the proposed multiview algorithm is less sensitive to noise than the corresponding monoview one.

IV. CONCLUSIONS

A multiview microwave imaging process for a 2-D infinite cylinder has been developed, and its capabilities have been assessed and compared with those of a monoview algorithm. Results have demonstrated both the feasibility of reconstructing strong scatterers through a dielectric-reconstruction process and the possibility of forming the images of weak scatterers by using the values of the equivalent currents only.

A study of noisy processes has demonstrated the robustness of the multiview approach. Finally, the method has pointed out the dependence of the reconstruction process on many factors. In particular, the geometrical properties of the objects considered, their locations inside the region examined, and the positions of the measurement points are all important parameters to be taken into account in the reconstruction process. Also, in terms of these parameters, the multiview algorithm is less critical than the monoview one. The paper has dealt with simple cases; in the future, our work will be aimed at the imaging of more complex objects.

REFERENCES

[1] A. J. Devaney, "Geophysical diffraction tomography," *IEEE Trans. Geosci. Remote Sensing*, vol. GE-22, pp. 3–13, 1984.

[2] J. C. Bolomey, "Recent European developments in active microwave imaging for industrial, scientific, and medical applications," *IEEE Trans. Microwave Theory Tech.*, vol. 37, pp. 2109–2117, 1989.

[3] Y. Sakamoto, K. Tajiri, T. Sawai, and Y. Aoki, "Three-dimensional imaging of objects in accumulated snow using multi-frequency holography," *IEEE Trans. Geosci. Remote Sensing*, vol. 26, pp. 430–436, 1988.

[4] M. Slaney, A. C. Kak, and L. E. Larsen, "Limitation of imaging with first-order diffraction tomography," *IEEE Trans. Microwave Theory Tech.*, vol. MTT-32, pp. 860–873, 1984.

[5] R. F. Harrington, *Field Computation by Moment Method.* New York: Macmillan, 1968.

[6] D. K. Ghodgaonkar, O. P. Gandhi, and M. J. Hagmann, "Estimation of complex permittivities of three-dimensional inhomogeneous biological bodies," *IEEE Trans. Microwave Theory Tech.*, vol. MTT-31, pp. 442–446, 1983.

[7] M. M. Ney, A. M. Smith, and S. S. Stuchly, "A solution of electromagnetic imaging using pseudoinverse transformation," *IEEE Trans. Med. Imaging*, vol. MI-3, pp. 155–162, 1984.

[8] T. C. Guo and W. W. Guo, "Physics of image formation by microwave scattering," *SPIE Proc.*, vol. 767, 1987.

[9] S. Caorsi, G. L. Gragnani, and M. Pastorino, "Equivalent current density reconstruction for microwave imaging purposes," *IEEE Trans. Microwave Theory Tech.*, vol. 37, pp. 910–916, 1989.

[10] T. C. Guo and W. W. Guo, "Computation of electromagnetic wave scattering from an arbitrary three-dimensional inhomogeneous dielectric object," *IEEE Trans. Magn.*, vol. 25, no. 4, pp. 2872–2874, 1989.

[11] M. J. Hagmann and R. L. Levine, "Procedures for noninvasive electromagnetic property and dosimetry measurements," *IEEE Trans. Antennas Propagat.*, vol. 38, pp. 99–106, 1990.

[12] S. Caorsi, G. L. Gragnani, and M. Pastorino, "Image reconstruction by inverse-scattering solution for multiple microwave views," in *Proc. URSI Int. Symp. Electromagn. Theory* (Stockholm, Sweden), 1989, pp. 590–592.

[13] A. Korganoff and M. Pavel-Parvu, *Methodes de calcul numerique*, Tome 2, *Elements de theorie des matrices carrees et rectangles.* Paris: Dunod, 1967.

[14] J. H. Richmond, "Scattering by a dielectric cylinder of arbitrary cross-section shape," *IEEE Trans. Antennas Propagat.*, vol. AP-13, pp. 334–341, 1965.

[15] A. F. Peterson and P. W. Klock, "An improved MFIE formulation for TE-wave scattering from lossy, inhomogeneous dielectric cylinders," *IEEE Trans. Antennas Propagat.*, vol. 36, pp. 45–49, 1988.

[16] J. C. Bolomey, C. Pichot, and G. Gaboriaud, "Critical and prospective analysis of reconstruction algorithms devoted to a planar microwave camera for biomedical applications," in *Proc. URSI Int. Symp. Electromagn. Theory* (Stockholm, Sweden), 1989, pp. 144–146.

[17] D. S. Jones, *The Theory of Electromagnetism.* Oxford: Pergamon Press, 1964.